Numerical simulations of the mingling caused by a magma intruding a resident mush

Alexandre Carrara, Alain Burgisser, George W Bergantz

VOLCANICA

Numerical simulations of the mingling caused by a magma intruding a resident mush

Alexandre Carrara*[α,β,γ], Alain Burgisser[α], and George W. Bergantz[β]

[α] Univ. Grenoble Alpes, Univ. Savoie Mont Blanc, CNRS, IRD, UGE, ISTerre, 38000 Grenoble, France.
[β] Department of Earth and Space Sciences, Box 351310, University of Washington, Seattle, WA 98195, USA.
[γ] Université Clermont Auvergne, CNRS, IRD, OPGC, Laboratoire Magmas et Volcans, F-63000 Clermont-Ferrand, France.

ABSTRACT

Currently, our ability to interpret the mechanics of magma mingling and mixing is limited by an incomplete understanding of the modes of mixing across all melt fractions and compositions. Here, we present numerical simulations of the emplacement of crystal-free magma in crystal-rich reservoirs employing a computational fluid dynamics and discrete element method (CFD–DEM). We performed two runs corresponding to the emplacement of basalt into two end-member types of magmas mush (basaltic and dacitic). We found that the intruded volumes have similar shapes and are surrounded by a halo where the crystal volume fraction of the mush is lower. The dynamics of intruded melt are, however, different. Importantly, the mingling of the intruded and host materials starts after emplacement and consists in the incorporation of mush material into the intruded magma. Our findings imply that purely thermo-mechanical processes controlled by grain-scale dynamics are sufficient to explain fundamental aspects of recharge.

KEYWORDS: Magma reservoirs; Intrusion; Mingling; Magma; Mush; Numerical simulations.

1 INTRODUCTION

The replenishment of magma reservoirs by hotter and crystal-poor magmas is a widely observed process contributing to the formation and evolution of magma bodies in the upper crust [Wiebe 1996; Annen et al. 2015; Wiebe 2016; Karakas et al. 2017]. These events are also inferred to have a role in initiating the conditions that may lead to an eruption [Eichelberger and Izbekov 2000; Bachmann and Bergantz 2004; Burgisser and Bergantz 2011; Huber et al. 2011]. Eruptive products resulting from the rejuvenation of a reservoir by recharge in new magmas manifests either significant [e.g. Pallister et al. 1996; Murphy et al. 2000; Nakagawa et al. 2002; Pichavant et al. 2018] or limited mixing/mingling between the two magmas [e.g. Clynne 1999; Bachmann et al. 2002; Takahashi and Nakagawa 2013; Bachmann et al. 2014]. One obstacle in interpreting the diversity of geological expressions of magma mixing/mingling arises from an incomplete understanding of the complex dynamics of multiphase mixing/mingling. Following Jarvis et al. [2021], we employ the term 'mingling' as the physical juxtaposition and stirring of magmatic materials whereas 'mixing' refers to the chemical hybridation by diffusion of miscible elements. We use the term 'granular mixing' to express the dispersion of non-Brownian particles (crystals).

Magma mingling is a two-step process: (1) the initial juxtaposition of magmas by penetrative advection which sets the largest length scale, and (2) the reduction of that length scale by a stretching and folding circulation [Ottino 1989]. The juxtaposition of an intrusive magma and its host is inferred to result possibly from the buoyant ascent of the intrusion in the host [e.g. Bergantz and Breidenthal 2001; Ruprecht et al. 2008; Andrews and Manga 2014; Bergantz et al. 2015; Montagna et al. 2015; Schleicher et al. 2016]. The fingering of the interface

between the two magmas during the lateral emplacement of the intrusion is another mechanism of mingling [e.g. Snyder and Tait 1995; Perugini and Poli 2005]. The emplacement of a new and hot magma may also rejuvenate the host material trapped below the intrusion, which is expected to be buoyant and may in turn invade the intruded layer [Jellinek and Kerr 1999; Bain et al. 2013]. The entrainment of the host melt by viscous drag into the intrusion during the settling of host crystals has been observed experimentally [Renggli et al. 2016; Jarvis et al. 2019]. Finally, experiments at temperatures and pressures prevailing in magma reservoirs suggest that the rapid emplacement of a large volume of new magma may induce instabilities of the interface between the two materials, triggering enclave formation and hybridization [Laumonier et al. 2014]. Stirring in magma reservoirs is often assumed to be driven by either the entrainment caused by thermal convection in the host due to the heat provided by a hotter intrusion [e.g. Jellinek and Kerr 1999; Couch et al. 2001; Burgisser and Bergantz 2011; Huber et al. 2011; Andrews and Manga 2014], or by vortices generated by the advection of the buoyant intruder in the host [e.g. Bergantz and Breidenthal 2001; Bergantz et al. 2015; Montagna et al. 2015; Schleicher et al. 2016].

In the context of crystal-rich (mushy) reservoirs, a network of frictional contacts can form which produces a sequence of fragile states up to full lock-up [Bergantz et al. 2017]. This rheological lock-up imposed by the crystal network inhibits or delays the generation of convection in the host mush [Burgisser and Bergantz 2011]. Numerical simulations of the injection of a crystal-free magma into a mush accounting explicitly for the presence of crystals have shown that the dynamics of the emplacement of an intrusion is controlled to first order by the density contrast between the two melts rather than the difference between their bulk densities [Carrara et al. 2020]. This restricts the scenarios where the buoyant intruder

ascends into the host to cases in which the host melt is either denser or neutrally buoyant with respect to the intruded one, or in which the host material has a yield strength supporting the upward propagation of a dike. The analysis of the physical properties and mingling and mixing efficiency of well-documented eruptions involving an intrusion and a mush suggests that efficient mingling and mixing are obtained when the intruded melt is denser [Carrara et al. 2020], and when the strain rate of emplacement is high enough to compensate the hindering effect of having a large viscosity contrast between host and intruder [Laumonier et al. 2014]. This suggests that mingling between the two materials requires the rapid emplacement of the intrusion. At low strain rates, the intrusion is expected to be emplaced as an horizontal layer at the base of the crystal-rich reservoir. Such underplating of a (generally) mafic intrusion is expected to provide heat and possibly exsolved volatiles [Bachmann and Bergantz 2006] to the overlaying mush and may progressively rejuvenate the reservoir but is not expected to result in significant incorporation of the intruded material into the host mush nor in extensive mingling between the two materials [Bergantz 1989; Bachmann and Bergantz 2004; Burgisser and Bergantz 2011; Huber et al. 2011]. Hence the processes governing the mingling between the host mush and its denser intruder are still unclear because of our partial understanding of the host–intrusion interactions during the syn- and post-intrusion phases. In other words, we have an incomplete grasp of when and where the two materials will start to significantly interact and generate a dynamics resulting in their progressive hybridization.

To explore how a magma mush may mingle with a denser intrusion, we performed numerical simulations using a Computational Fluid Dynamics and Discrete Element Method (CFD–DEM) model accounting for the heat exchanged between the two magmas and for the associated evolution of their density and viscosity. Simulations consist in the rapid emplacement and relaxation of a volume of crystal-free basalt into either a basaltic or a dacitic mush. We describe and compare the dynamics of the crystals and melt phases in the two simulations. We then discuss the implications of our results on the understanding of the physical processes governing the mingling between the two materials.

2 METHOD

To explore the dynamics generated by the intrusion of magma into a host mush, we performed CFD–DEM numerical simulations by using the `MFIX–DEM` software*. CFD–DEM is able to model the coupled dynamics of melt and crystals accounting for the interphase exchanges (heat and momentum) and contacts among the solids (considered as spheres here). The dynamics of the liquid phase is computed by solving the conservation of mass, momentum, and energy considering an incompressible liquid and using the Boussinesq approximation. The motion of each crystal is modeled by applying external forces (buoyancy, drag, and contacts) to it and solving Newton's second law. To compute the drag force, we use the modifications introduced in Burgisser et al. [2020] to account for the

---

*https://mfix.netl.doe.gov/
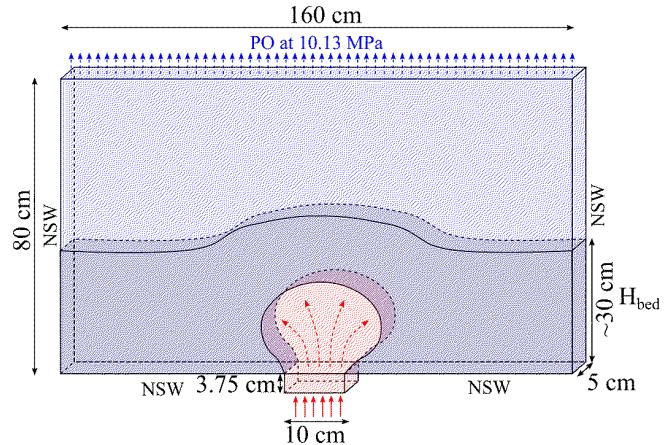
Figure 1: Simulation setup view from the side. The background color depends on the composition. The blue area indicates the host liquid. The red domain corresponds to the volume occupied by the intruded liquid. The grey/blue area indicates the location of the particle bed forming the layer of mush. The intruded liquid is crystal-free and initially occupies the small conduit at the base of the reservoir. The solid red arrows indicate the direction in which the injection of the intruded liquid is imposed. The dashed blue arrows indicate the fixed pressure outflow located atop the domain. The dashed red arrows indicated the expected flow of the injected liquid. The expected growth of the intrusion and associated liquid flow are deduced from Carrara et al. [2020]. Except for the inlet, pressure outflow, and the front and back of the reservoir (cyclical boundary conditions), we employed non slip wall as boundary conditions.

high liquid viscosities relevant to magmas while avoiding an unrealistic computational cost. Details about the theory and implementation of the model are presented in Syamlal et al. [1993], Syamlal [1998], Garg et al. [2012], Li et al. [2012], and Carrara [2019]. A detailed list of the equations can be found in Supplementary Material 1.

Simulations consist in the injection of a crystal-free magma into a mush (Figure 1). The composition and temperature of the intruded melt are different from that of the host, which induces density and viscosity contrasts. The evolution of the local composition of the melt during the simulations is tracked using the transport equation of a scalar compositional index that represents the fraction of the two melts [Carrara et al. 2020]. The compositional changes resulting from chemical diffusion are neglected because the duration of the simulations are short compared to the diffusion timescale. The validation of the ability of the model to capture the dynamics and hybridization of two miscible liquids having density and viscosity contrasts can be found in Carrara et al. [2020] and Molina et al. [2012]. The influence of temperature changes on the density and viscosity of the two melt phases is computed using two state equations. The first equation expresses the thermal expansion of the melt phases at constant pressure:

$$\left(\frac{\partial \rho_l}{\partial T_l}\right)_P = -\alpha_l \rho_l \tag{1}$$

where α_l is the coefficient of thermal expansion of the melt (considered to be independent of composition and temperature here), ρ_l is the melt density, and T_l is the melt temperature. The evolution of the size and density of the crystals with temperature are neglected because their coefficient of thermal expansion is too small to influence the dynamics of our simulations and because simulation times are short compared to crystallization–dissolution kinetics. The melt viscosity is computed as a function of composition and temperature as [Giordano et al. 2008]:

$$\log_{10} \eta = -4.55 + \frac{B}{C + T_l} \qquad (2)$$

where η is the dynamic viscosity of the melt, B and C are two constants depending on the chemical composition. During the simulations, the local value of the coefficients B and C are updated as a function of composition by considering an ideal mixture between the two melts.

We employ the same geometry as that of the simulations presented in Carrara et al. [2020]. The reservoir consists in a 3D rectangular tank of $1.6 \times 0.8 \times 0.05$ m (length × height × width) filled with a viscous liquid (Figure 1). We use a grid resolution of 1.25 cm for the liquid phase. A ~0.3 m thick mush layer is located at the base of the reservoir. The crystals are initially generated at random positions and settled in the vacuum to avoid the segregation of the mineral species having different densities in distinct layers during the settling. We use three slightly different sphere diameters to represent the crystals (4.5, 5, 5.5 mm) to avoid artificial self-organization of the solids. The intruded melt is injected at the base of the mush layer with a constant flux through a 3.75 cm long and 10 cm wide conduit such that the intruded melt enters the mush as a Poiseuille flow [Carrara et al. 2020]. We emphasize that the dimensions of the tank in the simulations are far below those expected for magma reservoirs. We chose to use these dimensions to use realistic particle sizes so that the dimensionless numbers controlling the exchange of momentum between the crystals and the viscous melt [Stokes and particle Reynolds number, Bergantz et al. 2017] are in the same range as those encountered in magmas. Accounting for a larger tank in the simulations without increasing the number of particles and the computational costs, would have compelled us to use larger crystals for which the fluid-solid coupling is not relevant to magmas.

We performed two simulations representing end-member scenarios common in arc magmatism. The first simulation (A) investigates the intrusion of basaltic melt into a basaltic mush whereas the second scenario (B) corresponds to the replenishment of a dacitic reservoir with a basaltic melt. For both simulations, we choose the chemical composition of the magmas such that the intruded melt is denser and less viscous than the host one, which corresponds to conditions where efficient mingling is observed in nature [Carrara et al. 2020]. For simulation A, we computed the physical properties of the melt and crystal contents of the host mush by simulating the cooling and crystallization of a basaltic magma using the MELTS model [Ghiorso and Sack 1995; Asimow and Ghiorso 1998] in the software PELE [Boudreau 1999] at a pressure of 250 MPa.

The chemical composition of the basaltic melt at liquidus is taken from Dufek and Bachmann [2010] (see Table 1 for chemical compositions and physical properties of the intruded and host materials). The intruded melt is the same magma at liquidus. In simulation B, the chemical compositions and crystal contents of the two materials were extracted from Caricchi and Blundy [2015] (dacitic mush) and Melekhova et al. [2013] (basalt). We consider four minerals species (plagioclase, olivine, clinopyroxene, and biotite) having different densities (2700, 3300, 3400, and 3500 kg m^{-3}, respectively). The respective proportions in the different mineral groups composing the mush layers are taken from the results of the MELT simulation (Simulation A) or Caricchi and Blundy [2015] (Simulation B). For the initial conditions, the temperature, density, and viscosity of the host liquid are considered as uniform. The initial pressure of the liquid is computed by the model at the first timestep from the pressure we imposed at the upper boundary conditions. The liquid and particles are considered to be at rest. The temperature, density, and viscosity at the initial condition for each simulation is indicated in Table 1.

We scale the injection velocity and simulation time using the relationships detailed in Carrara et al. [2020]. The dimensionless injection velocity, U^*, corresponds to the ratio between the injection velocity, U_{inj}, and the minimum fluidization velocity, U_{mf}, which corresponds to the injection velocity at which the upward hydrodynamic forces equal the reduced weight of the crystal layer [Schleicher et al. 2016; Carrara et al. 2020]. The dimensionless time [Bergantz et al. 2017], t^*, corresponds to the ratio of the simulation time, t, over the time needed for the injected melt to flow across the thickness of the mush layer, t' ($t' = H_{bed}/U_{inj}$, where H_{bed} is the mush layer thickness). The dimensionless time is useful to compare simulations with the same mush layer but different physical properties (density and viscosity) because it is proportional to the injected volume [Carrara et al. 2020].

To test the hypothesis that a high strain rate promotes mingling between the two magmas, we use the same dimensionless injection rate ($U^* = 93470$) for which the geometry of the intruded layer is dominated by the momentum resulting from the injection. For the simulation with the basaltic mush, the injection Reynolds number, Re ($Re = \rho_l U_{inj} W_{inj}/\eta$), is ~$1 \times 10^{-2}$ and the viscosity contrast is ~10 such that some mixing is expected between the host and intruded materials [Jellinek et al. 1999]. For the run with the dacitic reservoir, Re is ~1×10^{-6} and the viscosity contrast of ~1×10^4 for which no mixing is expected. For such high U^*, the intrusion is expected to grow primarily radially from the inlet [Carrara et al. 2020]. In both simulations, we kept the injection rate constant until $t^* = 1.17$. The dimensionless time $t^* = 1.17$ translates into different duration in the two simulations ($t = 7$ s in simulation A and $t = 699$ s in simulation B) because the difference in the physical properties of the host mush results in orders of magnitude of difference between the minimum fluidization velocities of the two simulations. The short duration of the injection in A allowed us to continue the simulation to explore the evolution of the interaction between host and intruded materials shortly after emplacement. After the injection is turned off at $t^* = 1.17$ ($t = 7$ s), the simulation continues until $t^* = 83.9$

Table 1: Chemical compositions and physical properties of the magmas in the simulations. pl., ol., bi., and cpx. correspond to plagioclase, olivine, biotite and clinopyroxene.

Parameter	Mush run A[1]	Intrusion run A[1]	Mush run B[2]	Intrusion run B[3]
Chemical compositions (wt.%)				
SiO_2	54.69	48.39	74.97	45.37
TiO_2	0.6	0.98	0.14	0.7
Al_2O_3	18.85	16.93	14.23	13.88
FeO(T)	5.41	10.07	0.93	7.30
MnO	0.48	0.18	0.08	0.34
MgO	1.12	5.96	0.24	13.63
CaO	4.77	10.46	1.29	10.30
Na_2O	4.78	2.67	2.68	2.23
K_2O	3.32	1.20	5.44	0.14
P_2O_5	0.59	0.22	0	0.08
H_2O	5.39	1.95	6.08	4.5
Melt physical properties				
T (°C)	925	1150	800	1200
Density ρ_l (kg m^{-3})	2305.1	2570.0	2036.97	2429.96
Dynamic viscosity η (Pa s)	366.52	11.21	5.912×10^4	1.835
Thermal expansion coef. α (K^{-1})	1×10^{-4}	1×10^{-4}	1×10^{-4}	1×10^{-4}
Thermal conductivity k_l (W m^{-1} K^{-1})	1.5286	1.5286	1.5286	1.5286
Heat capacity C_{pl} (J K^{-1})	1367.4	1367.4	1367.4	1367.4
Crystal physical properties				
Initial solid volume fraction ϕ_0	0.64	0.0	0.64	0.0
Mineral species	53–20–27 (pl–ol–cpx)	— —	75–17–8 (pl–bi–cpx)	— —
Density ρ_s (kg m^{-3})	2700–3300–3400 (pl–ol–cpx)	— —	2700–3300–3400 (pl–bi–cpx)	— —
Thermal conductivity k_s (W m^{-1} K^{-1})	2.4863	—	2.4863	—
Heat capacity C_{ps} (J K^{-1})	11 146	—	11 146	—
Injection				
Injection velocity U_{inj} (m s^{-1})	—	4.839×10^{-2}	—	5×10^{-4}
Dimensionless injection velocity U^*	—	93 470	—	93 470

Chemical compositions were taken from:
[1] Dufek and Bachmann [2010]
[2] Caricchi and Blundy [2015]
[3] Melekhova et al. [2013]

(t = 527 s). Reaching the same dimensionless duration in simulation B would have required an unrealistically long computation (~1.5 yr with the same computational power as for simulation A).

To quantify and locate granular mixing in our simulations, we computed the Initial Neighbor Distance (IND) mixing index presented in Schleicher et al. [2016]. This index quantifies the efficiency of the mixing among the crystals. It corresponds to the ratio between the sum of the distances that separate each crystal from its initial nearest neighbor, and the sum of the distances between each crystal and a random one. IND is zero when the crystal network remains the same as the initial one, and tends toward 1 when the mush layer is fully reorganized.

3 RESULTS

Figure 2 displays time-frames of simulation A at the dimensionless time t^* = 1.17 (t = 7 s). The intruded volume grows radially (Figure 2) as expected because of the large dimensionless injection velocity we imposed. The relaxation of the initial overpressure imposed by the initiation of mass inflow at the inlet (~1000 Pa above the injected material) results in the dilation of the crystal framework that forms a halo surrounding the injected volume (Figure 2A). The fluid flow is radial with velocities that are maximum above the inlet and decrease away from it (Figure 2C). The temperature of the melt decreases radially from the inlet and shows a diffusive pattern because of the diffusion of the intrusion heat to the host material (Figure 2D). Except a few crystals located near

the edges of the intrusion at the reservoir floor, no solids from the host are present in the intruded volume at that time (Figure 2E). The solids located in the host and above the intrusion show an upward flow, whereas the ones located on the side of this volume have no significant vertical motion.

Simulation B displays the radial growth of the intrusion surrounded by a halo where the crystallinity is lower (Figure 3A), as in simulation A. The shape of the intrusion is nevertheless a little more elongated horizontally (Figure 3B) than in simulation A (Figure 2B). The flow of the melt is, however, significantly different from simulation A and shows convection within the intrusion (Figure 3C). The intruded material starts to convect once $t^* > 0.5$. Hot melt ascends atop the inlet and colder material sinks from the interface between the two materials, which results in concentrating the temperature gradient at the margin of the intrusion (Figure 3D). The cooling of the intruded melt at the margins of the intrusion (Figure 3D) results in the increase of the melt viscosity in a buffer layer circumscribing the convection within the intrusion (Figure 3C). As a result, the convective flow is unable to stir the surrounding mush, where the melt and crystals flow radially away from the intrusion (Figure 3C, E) as in simulation A. Antecrysts are found within the intrusion (Figure 3E) because of the progressive settling of the crystals located above the intrusion. They tend to accumulate at the inlet.

In both simulations, two important phenomena occur in the mush. The first is that the pressure gradient in the bed at rest follows closely that expected if no particles were present (Figure 4A). In other words, the pressure at the base of the bed is close to the hydrostatic pressure based on melt density but it is smaller than the hydrostatic pressure based on bulk density (i.e. the pressure gradient if the bed were in a fluidized state). This underpressure with respect to the fluidized state results from the particle network which supports the reduced weight of the particle bed because of normal forces being heterogeneously transmitted by force chains through particle contacts. Such force chains are, like in other hydrogranular media, split into a strong network parallel to the gravitational loading and a weak load-carrying network that is mostly isotropic acting as a kind of granular pressure [Bergantz et al. 2017]. Thus, depending on which network particles at the base belong to, there is a pressure difference of up to 1×10^3 Pa between these particles and the surrounding melt. The injection of new melt not only fluidizes the overlying mush but also induces a pressure increase in the melt that exceeds the hydrostatic pressure gradient based on bulk density (Figure 5). In both runs, the overpressure is maximal at the beginning of the simulation and decreases as the injection proceeds (Figure 5B–C). Force chains with a main direction parallel to fluid flow are formed where the overpressure is largest, resisting the radial motion. This local maximum of overpressure occurs at some distance from the mush/intrusion interface. As a result, particles located between the intrusion and the maximum overpressure cease to belong to the solid network and the dilute halo forms. These isolated particles follow the fluid radial motion, but they lag behind the propagation of the dilute halo because they no longer form a coherent network with the rest of the bed. The ensuing consequence is that hindered settling relative to the

fluid occurs in this dilute halo. Because the settling velocity of particles at low volume fraction is faster than that at high volume fraction, particles spread and create a gradient in solid volume fraction (ϕ) (Figures 2A and 3A).

We delimited the dilute halo as the region where $0.1 < \phi < 0.52$ and containing >50% of the resident melt minus the sliver of mush atop the bed that fulfills these conditions at $t^* = 0$ (i.e. when there is no injected melt). The volume of the dilute halo is about 2.5 times that of the injected melt, regardless of time (Figure 6). The appearance of this dilute part in an otherwise packed bed implies that host melt was drawn into the bed from the particle-free region above the bed. We calculated this volume of additional melt by volume balance. Because particle volume is constant, the volume of melt drawn in is the bed volume ($\phi > 0.1$ and $\phi < 50\%$ of resident melt) minus the initial bed volume. This additional melt drawn into the mush is about 0.9 times that of the injected melt, regardless of time (Figure 6). The differential velocity between particles and melt shows that melt is entrained into that halo by tortuous permeable flow (Supplementary Material 2 Figure S1). This process impacts the way that the bed top surface bulges. We define the bulge volume as the region with $\phi > 0.1$ that is above the initial bed surface. Instead of having a volume comparable to that of the injection, the bulge is ~1.9 times larger than the intrusion (Figure 6) because of the additional melt migrating from above the bed into the dilute halo. To develop freely as observed, the dilute halo thus needs that the packed bed is surrounded by a dilute region that is at least twice the volume injected. Defining the available melt as the amount of melt that can be drawn from a dilute region without creating a packed bed, this dilute region (here particle-free) must contain at least 0.9 times the injected volume of available melt.

Figure 7 displays time-frames of the evolution of the crystal content, chemical composition, and temperature of simulation A after the injection was stopped ($t^* = 1.17$) and until $t^* = 83.9$ ($t = 527$ s). Once the injection ceases, the evolution of the geometry of the intrusion becomes controlled by the buoyancy contrast between the two melts. The intruded melt starts to pond over at the base of the reservoir to form an horizontal layer (Figure 7B, H, N). Widespread incorporation of host crystals into the intrusion occurs after we stopped the injection. The increasing number of antecrysts into the intrusion results from two mechanisms. First, a portion of the host mush is trapped below the intrusion during its lateral spreading. The trapped host melt is buoyant with respect to the intruded melt and invades the intrusion, forming Rayleigh-Taylor instabilities and entraining crystals (~30%–40% in volume; Figure 7C–F). Later, when the lateral spreading is slower, host crystals located in the dilute halo atop the intrusion progressively settle into the intrusion. We expect that full settling happens eventually, at a time that far exceeds the full duration of the simulation. The intrusion progressively cools (Figure 7M–R) because of the diffusion of heat into the mush, the incorporation of crystals at thermal equilibrium with the host melt, and the advection of the colder material trapped below the intrusion (Figure 7O–R).
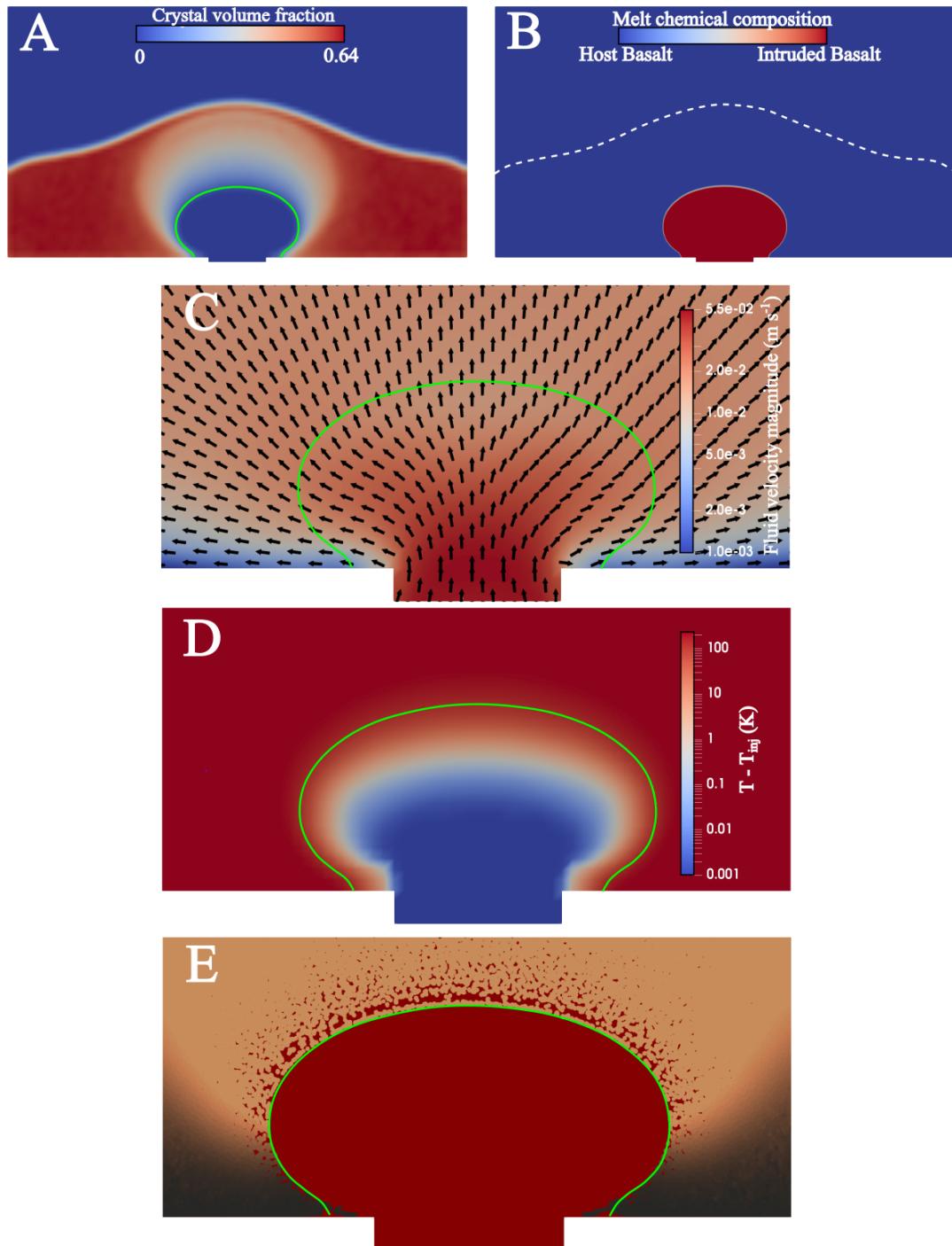
Figure 2: Snapshots of simulation A at $t^* = 1.17$ ($t = 7$ s). In [A] and [C–E], the green curves represent the boundary between the host and intruded melts deduced from snapshot B. [A] Distribution of crystal volume fraction. [B] Composition index of the melt. The white dashed curve indicates the location of the top of the mush layer, taken at $\phi = 0.4$ in the inset A. [C] Flow field of the melt. Black arrows indicate the direction of the flow. The velocity magnitude is given by the background color. [D] Difference between the local and intrusion temperature. [E] Vertical velocity of the crystals. Each disc represents a particle. Particles colored in beige move upward and particles displayed in black have negligible vertical velocities.
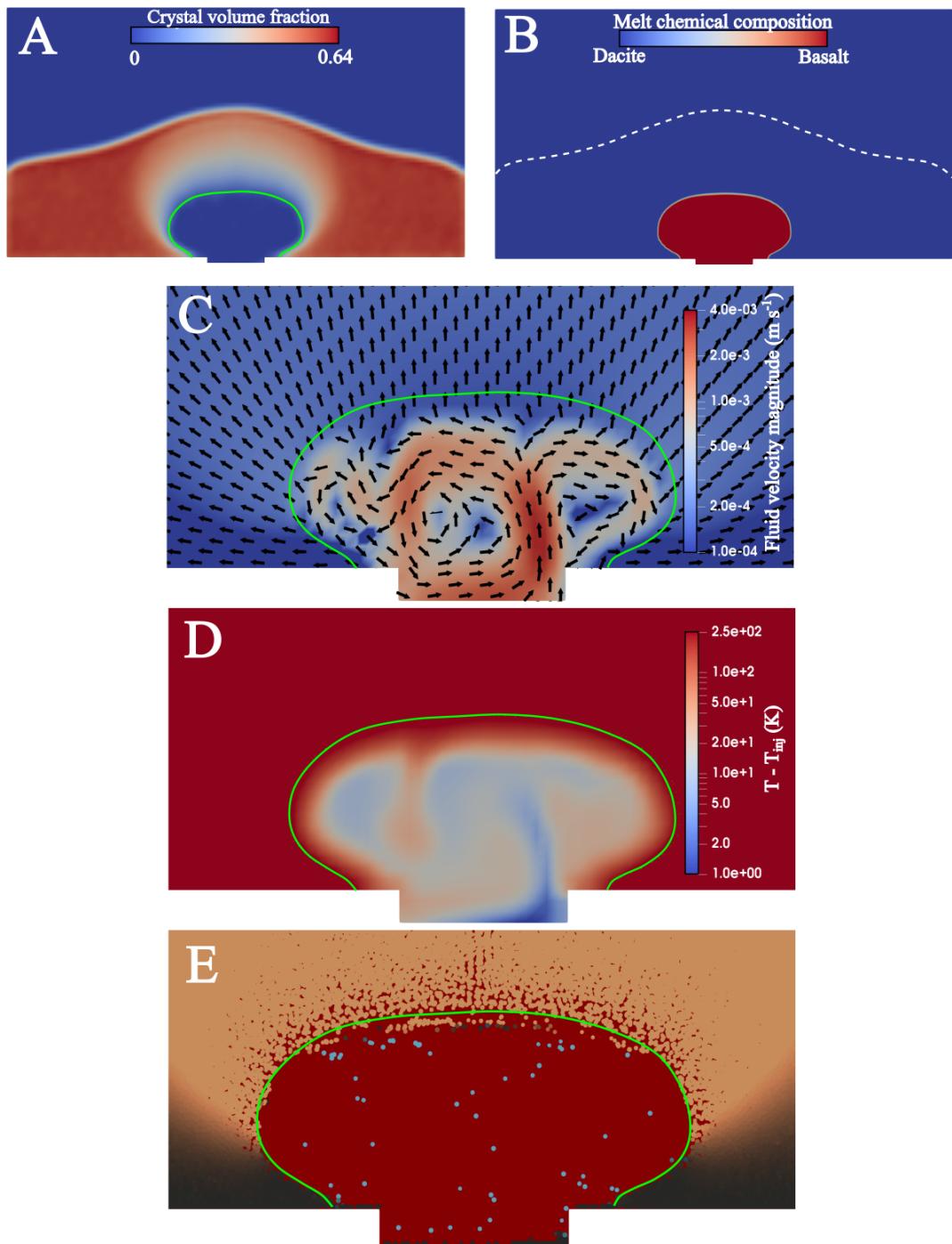
Figure 3: Same as Figure 2 for simulation B at t^* =1.17 (t = 699 s). In [E], the particles colored in cyan have a downward motion.

Once injection stops, the dilute halo deforms itself in a complex shape following the laterally spreading intrusion. Particles forming the gradient in solid volume fraction settle slowly (Figure 7A–F). The halo volume does not change during the spreading. We also observe the progressive decrease of the average crystals content in the mush located above the diluted halo (Figure 7A–F). At $t^* = 1.12$, the crystal content of the mush is typically >60%, whereas at $t^* = 83.9$, it is <60% (at most ~58%). Despite the decrease of the crystal volume fraction, contacts are still present within the mush surrounding the dilute halo (Figure 8A). A strong decrease in crystal

content is also observed in the mush above the inlet but it artificially results from the finite sizes of the particle bed and the computational domain. The average Initial Neighbor Distance of the crystals at $t^* = 83.9$ is IND = 0.0114, indicating a limited reorganization of the crystal network during and shortly after the intrusion. The spatial evolution of the IND shows that most of the granular mixing occurs within the intruded layer (Figure 8B). In the mush layer surrounding the intruded layer, the two granular vortexes are not able to generate a significant granular mixing of the host crystals, which flow as a bulk. Restricting the computation of the IND to the crystals
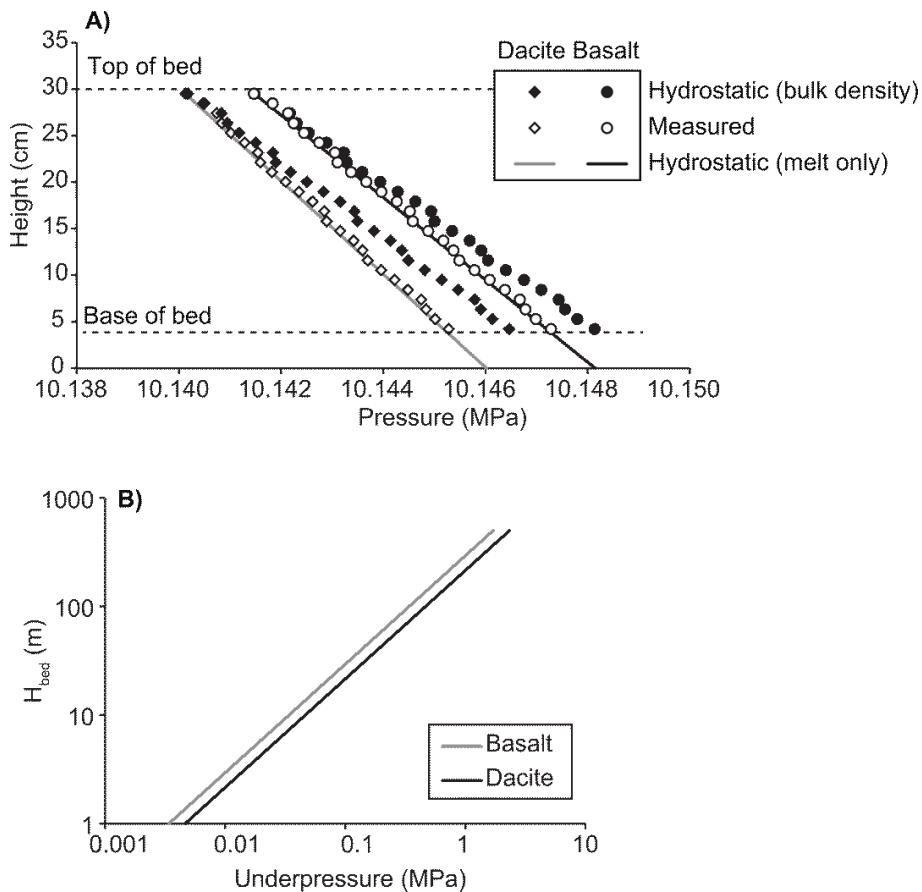
Figure 4: [A] Pressure values along a vertical line located in the particle bed at x = 10 cm, z = 2.5 cm. Values depicted by symbols are from run A (diamonds) and B (circles). They are either measured (open symbols) or recalculated based on bulk density (closed symbols). Lines are based on the pressure gradient of a pure melt (gray: run A with ρ_l = 2305 kg m^{-3}; black: run B with ρ_l = 2037 kg m^{-3}. Dashed horizontal lines indicate the position of the bed top and base. [B] Amount of underpressure at the base of a mush as a function of mush thickness. Values of melt density and average crystal density are taken from run A (basalt) and B (dacite).

located in the intrusion (where the composition index is above or equal to 0.5) at t^* = 83.9 gives IND = 0.106, whereas only considering the crystals located in the mush gives the much lower value of 0.0083.

4 DISCUSSION

Our simulations illuminate the diversity of interactions existing between the intrusion and an existing mush, with a specific focus on the physical mechanisms responsible for their mingling during and shortly after emplacement. We used initial compositions in which the intruded melt is denser than the host liquid so that emplacement occurs as an horizontal layer at the base of the mush. This corresponds to the scenario where efficient mixing/mingling is observed between the intrusion and the host mush [Carrara et al. 2020]. In both simulations, mingling was not observed during emplacement (Figures 2B and 3B). In run A, mingling initiated after the injection was stopped and was caused by the ascent of mush materials trapped below the intrusion during its lateral spreading (Figure 7). Such gravitational instabilities are observed in mafic-felsic layer complexes [e.g. Bain et al. 2013; Wiebe 2016], and have been interpreted to be triggered by the thermal re-

juvenation of a layer of mush located below the intrusion and in which a yield stress exists [Jellinek and Kerr 1999; Bain et al. 2013]. Our simulations show that such instabilities may also be triggered by the rapid emplacement of an intrusion in a reservoir where the host does not have any yield stress. Regardless of its trigger, the ascent of host material trapped below the intrusion results in the progressive incorporation of mush material into the intrusion.

Other mechanisms responsible for the juxtaposition of two magmatic materials have been described in the literature but do not occur in our simulations. The fingering of the interface between the mush and the intrusion during its lateral spreading [e.g. Snyder and Tait 1995; Perugini and Poli 2005] also results in the incorporation of host material into the intruded magma. According to Snyder and Tait [1995], and considering the physical properties of the host melt, the expected widths of the finger in our simulations are ~74 cm in simulation A and ~91 cm in B. The presence of the crystals in the mush increases the effective viscosity of the host material and in turn the width of the fingers. As a result, the estimate of the finger width with the melt properties represents an estimation of the minimum width of the fingers, which far exceed the width of
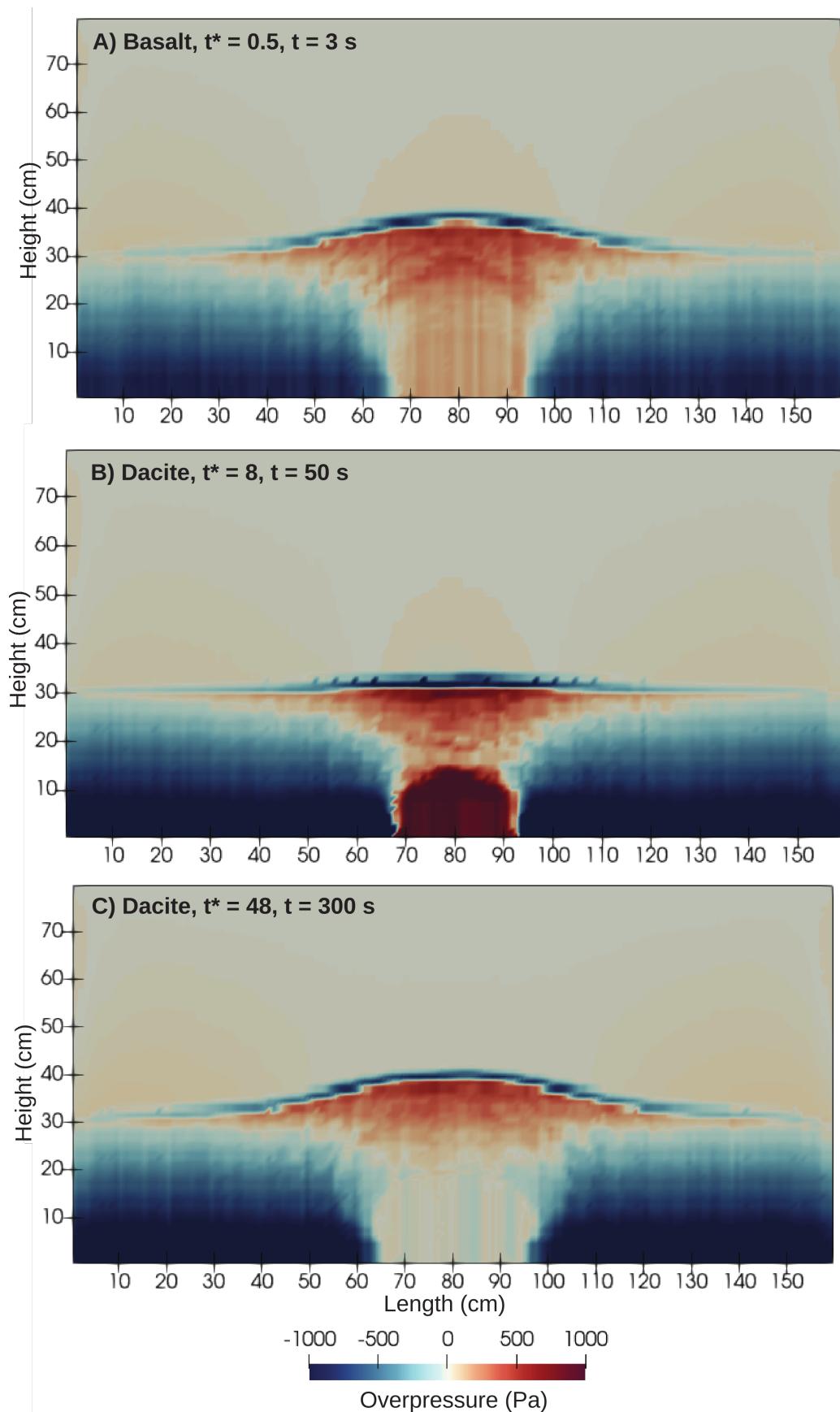
Figure 5: Cross sections at mid-thickness (z = 2.5 cm) of the overpressure distribution. The overpressure is defined as the fluid pressure minus the hydrostatic pressure based on the local bulk density. [A] Run A at t^* = 0.5. [B] Run B at t^* = 0.8. [C] Run B at t^* = 0.50.
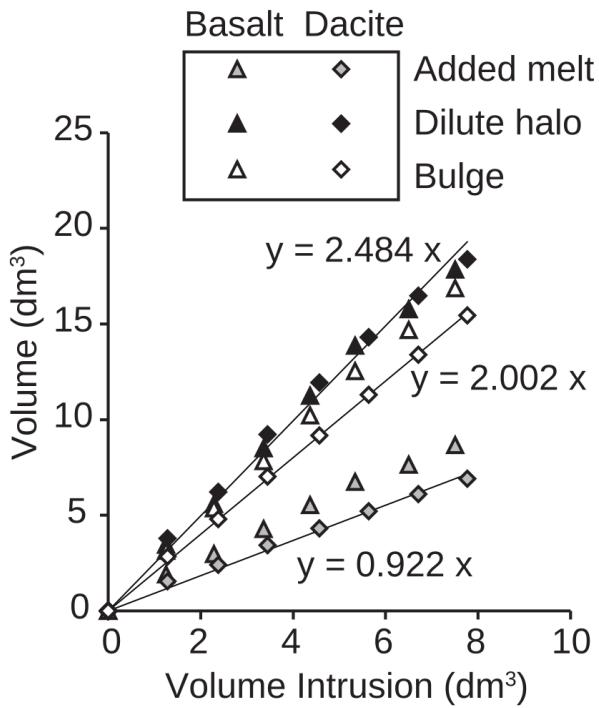
Figure 6: Volume of three elements within the resident mush as a function of intruded volume. Black symbols represent the dilute halo, which is the part directly above the intrusion with a gradient of particle volume fraction. Gray symbols represent the added melt, which is the volume of melt added into the dilute halo by permeable flow. White symbols represent the bulge, which is the mush volume located above the initial bed surface. Data are from $t^* = 0$ to $t^* = 1.17$ for both run A (basalt) and run B (dacite). The three regression lines are based on run B; their squared coefficients of Pearson product moment correlation are >0.997.

our reservoir (∼5 cm) explaining why they are absent. The estimated size of the fingers is also far above the grid resolution we employed (1.25 cm) so their absence is not related to the coarse grid we employed. Provided that fingering in dense suspensions can adequately be represented by pure liquids as in the work of Snyder and Tait [1995], we expect fingering to occur during the lateral spreading of the intrusion if the simulations were run with a larger width, which would cause further incorporation of host materials into the intrusion. After stopping the injection in run A and during injection in run B, we observed crystals settling from the host and invading the intrusion (Figures 3E and 8A). Entrainment of the host melt resulting from the settling of crystals through the interface between two stratified liquids having a viscosity contrast has been observed experimentally [Renggli et al. 2016; Jarvis et al. 2019]. The width of the entrained liquid at the tail of the particle is, however, smaller than the diameter of the settling particles. As a result, this mechanism is not present in our simulations because of the size of our liquid cells is too coarse (2.5 times the average particle diameter). We expect that this phenomenon would have occurred in the simulations if they

were run with a fluid mesh smaller than the size of the particles [e.g. Culha et al. 2020], which would have contributed to further entrainment of the host melt into the intrusion.

Laumonier et al. [2014] argued that the rapid emplacement of an intrusion of large volume would generate a high strain rate (in simple shear) able to trigger the mingling between two magmas having a large viscosity contrast because mingling is hindered by large viscosity contrasts at low strain rates. In both simulations, we used viscosity contrasts that are expected to hinder mingling at a low strain rate [>0.3 log units, Laumonier et al. 2014] and a high injection rate. At such injection rate, the geometry of the intrusion is controlled by momentum and grows radially from the inlet [Carrara et al. 2020]. As a result, the intrusion imposes a nearly pure shear to the mush during the injection, which is unable to destabilize the interface between the two materials. After the injection stops, the lateral spreading of the intrusion entrains two counter-rotating vortices in the mush that generate a downward flow above the inlet. This lateral entrainment of the mush results in smoothing and decreasing the shear rate at the interface between the two magmas, which is therefore unable to generate the destabilization of the interface even if the presence of the dilute halo surrounding the intrusion and the diffusion of heat both decrease the bulk viscosity contrast between the two materials near the interface.

Most of the physical mechanisms responsible for the juxtaposition of two magmatic materials that are (or should have been) present in our simulations consist in incorporating host material into the intruder and tend to occur after the emplacement of the intrusion rather than during the injection. We also showed that convective stirring is much more likely to occur within the intrusion rather than within the host. As a result, our simulations suggest that the mingling between an intrusion and its host take place predominantly after emplacement and in the immediate vicinity of the intrusion.

Although we considered the difference in temperature between the two melts, it does not have significant effects on the dynamics of the intrusion of simulation A, which could have been deduced from the results of Carrara et al. [2020]. This is because the growth of the intruded volume is too fast for the intruder to convect and because the injection shut-off stops the heat supply. During the lateral spreading, the thinning of the intruded layer and ensuing heat diffusion into the overlying and underlying mush reduces the likelihood of convection in the intrusion. Because simulation B takes a longer time to reach $t^* = 1.17$ (699 s) and because of the lower viscosity of the injected melt, simulation B features convection within the intruded volume. Computational limitations did not allow us to explore the effects of this convection on the evolution of the interactions between the intrusion and its host. Convection tend to homogenize the temperature of the melt within the intruded volume and to concentrate the temperature gradient to the margin of this volume, which both increase the cooling rate of the intrusion [Huber et al. 2009], which enhances the heat flux provided to the mush [Jellinek and Kerr 1999]. The heat transfer between the intrusion and its host is expected to generate a thermal boundary layer in the mush above the interface with the intrusion where convection occurs [Snyder
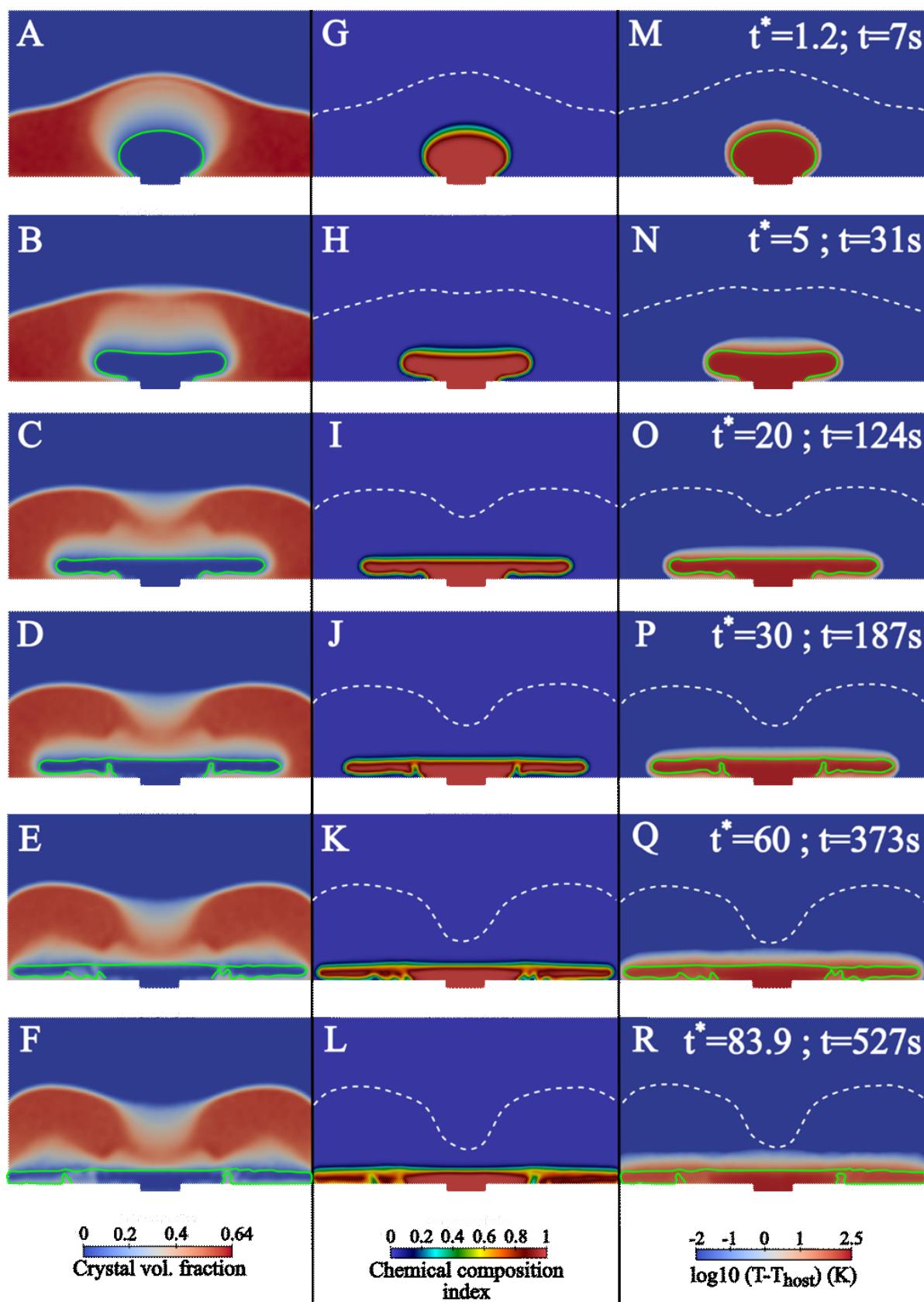
Figure 7: Evolution of the dynamics in run A after shutting off the injection. The solid green and dashed white curves indicate the interface between the two melts and the top of the particle bed, respectively. [A]–[F] Distribution of the content in crystals. The background color indicates the crystal volume fraction. [G]–[L] Chemical composition index of the melt. [M]–[R] Evolution of the difference of local temperature compared to the host initial temperature.
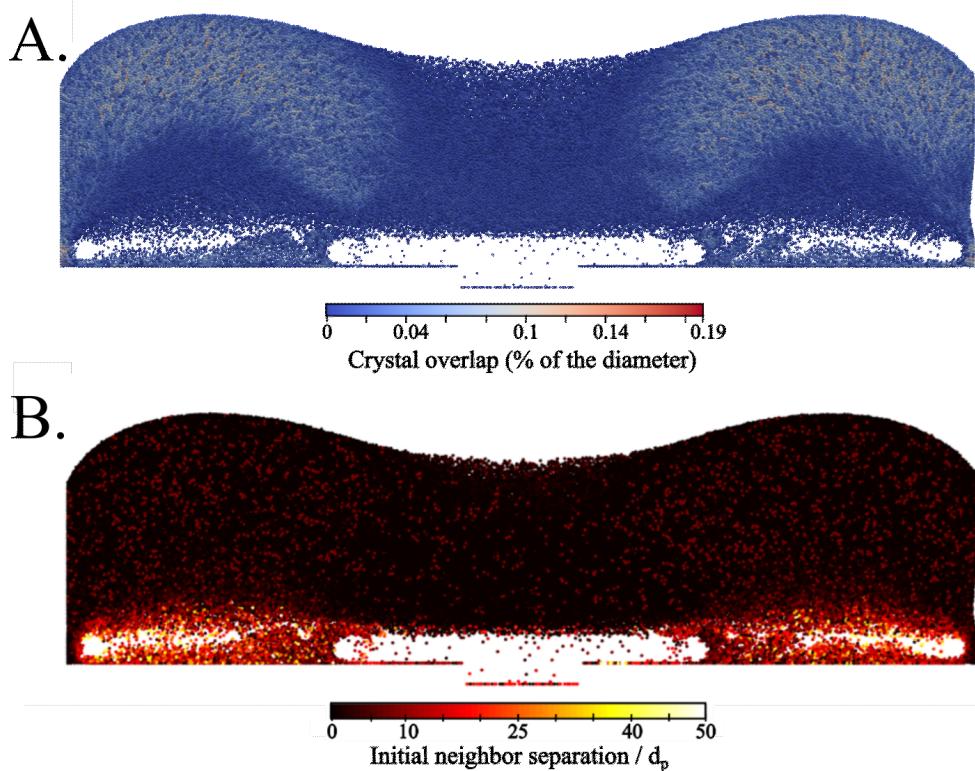
Figure 8: Snapshot of the particle dynamics in run A at $t^* = 83.9$. [A] Force chains network. The color of each particle depends on the maximum overlap distance with its neighbors normalized by its diameter. The overlap distance is a proxy for the magnitude of the contact force. [B] Distance separating each crystal from its initial closest neighbors normalized by the diameter of the particle (d_p).

2000]. Such thermal boundary layers have been inferred to become buoyant and result in reservoir scale overturn [Burgisser and Bergantz 2011]. In neither simulation is the heat supplied by the intruder able to generate a thermal boundary layer in the host mush. The Rayleigh number in the host thermal boundary layer that surrounds the intrusion (i.e. the mush that is affected by heat diffusion here) is of the order of 1×10^{-2}, far below the critical Rayleigh number at which convection starts ($\sim 1 \times 10^3$). According to the scaling relationship given in [Snyder 2000] for a continuous heat supply, the activation time for convection in the host material of simulation A is ~1150 s, which is longer than the full duration of our simulations and much longer than the time at which injection interruption stops heat supply. We thus do not expect convection in the host for $t^* > 83.9$, nor the vertical entrainment of intruded material by convection as observed in the experiments of Snyder and Tait [1996]. It follows that triggering thermal convection in the host mush would require the injection of a sufficiently large volume of magma to supply enough heat to the mush. An estimation of the thickness of such an intrusion based on a 1D model yields 0.2–83 m depending on magma composition [Burgisser and Bergantz 2011]. Furthermore, the formation of a thermal boundary layer involved melting the mush crystals, which tends to change the composition of the surrounding melt and increase its density (while the bulk density tends to decrease). The occurrence of gravitational instabilities in the melt is controlled by the density contrast existing between the liquid and not the bulk density contrast [Carrara et al. 2020]. The change in melt density resulting from crystal melting therefore opposes the entrainment of thermal convection in the thermal boundary layer and large-scale overturn. As a result, the ability of an intrusion to generate convective motion in the host mush is unclear and requires further investigation.

Quantifying the volume of resident magma indirectly affected by the intrusion allows us to also define the limits of validity of our simulations. Our runs happened in an end-member of the open environment because the region above the particle bed was filled with a pure melt that could flow out of the top boundary freely. The observed re-injection dynamics, however, does not require such extreme conditions. As long as the dilute, open part of the system contains at least roughly the same amount (0.9 times) of available melt as the injected material, we expect that the dilute halo would develop and reorganize fabrics over a volume ~2.5 times larger than the intrusion. Drawing melt from the dilute part of the system can occur until the resulting increase in crystallinity reaches values close to maximum packing. This dilute part is thus also part of the resident material volume affected by the intrusion. Consider for example a mush bed overlain (or surrounded) by a more dilute magma with 40% crystals. This system can be considered open like in our simulations until the melt drawn from the dilute part increases crystallinity to a locked-up state where melt can no longer be drawn because of maximum

packing conditions. Setting aside for now that lock-up does not depend only on crystal volume fraction, the cut-off value of ϕ depends on the crystal shape and size distributions [e.g. Bergantz et al. 2017]. In this example, we set this limit, ϕ_l, to 50 vol.% crystals. An intrusion could reorganize this illustrative system as follows. Melt can be drawn from the dilute region to feed the halo up to 10 vol.% of the dilute magma volume (i.e. increasing crystallinity from 40 to 50 vol.%). This melt transfer will occur mostly because the original mush surface would bulge into the dilute magma, taking up to twice the equivalent intrusion volume, V_{int} (Figure 6). The final system will have become mushy everywhere except in the halo near the intrusion, where a crystallinity gradient would have been created. The total volume of mush affected by the intrusion, V_{aff}, is thus that of the halo, $0.9 \times V_{int}$, plus that of the dilute magma, V_{dil}. Using volume balance, the volume of dilute magma that goes from initial crystallinity, ϕ_0, to maximum packing, ϕ_l, is equal to:

$$V_{dil} = \frac{\phi_1}{\phi_1 - \phi_0} 0.9 V_{int} \tag{3}$$

The ratio of the volume of mush affected by the intrusion over that intruded is thus:

$$\frac{V_{aff}}{V_{int}} = 2.5 + 0.9 \frac{\phi_1}{\phi_1 - \phi_0} \tag{4}$$

The end-member open system with pure melt we simulated ($\phi_0 = 0$) has thus a ratio of 3.9 and the example above ($\phi_0 = 0.4$ and $\phi_1 = 0.5$) has a ratio of 7. Even without mingling, the intrusive process can thus affect a volume of resident mush far larger than that of the fresh magma input. Open system events thus occur unhindered if sufficient parts of the resident system are more dilute than the maximum packing conditions. Beyond the volume ratio quantified by Equation 4, the resident system cannot accommodate the injected volume in the fashion described by our simulations. This has implications for pluton construction, which can be illustrated with the emplacement geometry of the Torres del Paine Intrusive Complex (Chile). This tabular, 1.1 km-thick granitic complex is composed of three major units emplaced successively such that each unit was solidified when the next one was emplaced [Michel et al. 2008; Annen et al. 2015]. Each unit is composed of smaller metric to decametric sills featuring ductile contacts [Leuthold et al. 2012; Annen et al. 2015]. Our results imply that each sill emplacement could have affected up to a few previously emplaced (ductile) sills featuring crystal contents lower than the maximum packing fraction, compacting them to accommodate the new injected volume. This process of progressive compaction would cease when maximum packing is reached. A full assessment of such an intriguing emplacement mechanism necessitates including crystallization, which is currently beyond the capabilities of our model.

In our simulations, we do not consider the presence of exsolved volatiles. The decompression linked to the ascent of the intrusion induces volatile exsolution. The cooling of a wet mafic magma emplaced at the base of the reservoir is also expected to trigger the exsolution of volatiles by second boiling. The exsolution of volatiles in the mafic layer has been inferred

to cause entrainment of the intruded material into the host [e.g. Thomas and Tait 1997; Wiesmaier et al. 2015] in a fashion similar to that resulting from crystal settling. Volatile exsolution could also result in the overturning of the reservoir or ascent of the intruded material because of the decrease of the bulk density of the intrusion [e.g. Huppert et al. 1982; Ruprecht et al. 2008; Montagna et al. 2015]. These studies considered the evolution of the bulk density of the intruded magma and neglect the relative motion between the crystal and the surrounding melt. When the phases constituting the magma are allowed to have a relative flow, the dynamics of the reservoir is rather controlled by the density contrast between the melts [Carrara et al. 2020], which makes it unlikely that exsolved volatiles change the bulk dynamics. Furthermore, numerical modeling of the flow of exsolved volatiles in magma has shown that in static, crystal-rich conditions (as the host material in our simulations) the gas tends to flow in channels [Parmigiani et al. 2014; 2017], which enhance the ability of the volatiles to flow through the host mush and probably decrease the probability of overturning and entrainment of intruded melt into the host. Although the role of volatiles on mingling and reservoir dynamics remains unclear, the exsolution of gas by second boiling requires the cooling of the intrusion, which occurs on timescales exceeding the duration of our simulations. We thus do not expect that accounting for the exsolution of volatiles in our simulations would have changed the dynamics we observed during and immediately after the intrusion.

5 CONCLUSIONS

In this study, we employed a CFD–DEM numerical model to simulate the emplacement of an intrusion into a mush and show that their mingling most likely occurs post emplacement and within the vicinity of the intrusion. We performed two simulations representative of end-member scenarios that may be encountered in arc volcanism (emplacement of basalt into a basaltic mush and basalt into a dacitic mush). In both simulations, the rapid injection of the intruded magma did not result in syn-emplacement contamination and mingling but generated a dilute halo surrounding the intrusion. The mingling between the host and its intruder was initiated after the injection was shut off and resulted from the ascent of mush material trapped below the intrusion. Although we considered the temperature difference between the two materials, it did not generate convection into the mush but within the intrusion only. The gradient in solid volume fraction created in the dilute halo is an unexpected outcome of a situation where the injected melt does not mingle with the resident mush during emplacement. The origin of this halo is Reynolds dilatancy and its internal structure features a crystallinity gradient under the combined effects of hindered settling and permeable flow. Although this dilute halo is expected to be ephemeral, it creates a crystallinity gradient by melt migration, which is to our knowledge a process described here for the first time. This gradient is fed by melt coming from more dilute parts of the resident magma. This melt withdrawal concentrates the dilute part, rearranging the preexisting fabric. The disappearance of the halo by settling will also reorganize the crystals involved. Overall, the mush fabric will be affected over a vol-

ume that is at least 3.9 times larger than that of the intrusion without direct interaction with the intruding melt.

Author Contributions

Acknowledgements

Data Availability

Simulations outputs and modified subroutines for the MFIX software are available at https://doi.org/10.5281/zenodo.7351796.

Copyright notice

References

Andrews, B. J. and M. Manga (2014). "Thermal and rheological controls on the formation of mafic enclaves or banded pumice". *Contributions to Mineralogy and Petrology* 167(1). ISSN: 1432-0967. DOI: 10.1007/s00410-013-0961-7.

Annen, C., J. D. Blundy, J. Leuthold, and R. S. J. Sparks (2015). "Construction and evolution of igneous bodies: Towards an integrated perspective of crustal magmatism". *Lithos* 230, pages 206–221. ISSN: 0024-4937. DOI: 10.1016/j.lithos.2015.05.008.

Asimow, P. D. and M. S. Ghiorso (1998). "Algorithmic modifications extending MELTS to calculate subsolidus phase relations". *American Mineralogist* 83(9–10), pages 1127–1132. ISSN: 0003-004X. DOI: 10.2138/am-1998-9-1022.

Bachmann, O. and G. W. Bergantz (2004). "On the origin of crystal-poor rhyolites: Extracted from batholithic crystal mushes". *Journal of Petrology* 45(8), pages 1565–1582. ISSN: 1460-2415. DOI: 10.1093/petrology/egh019.

– (2006). "Gas percolation in upper-crustal silicic crystal mushes as a mechanism for upward heat advection and rejuvenation of near-solidus magma bodies". *Journal of Volcanology and Geothermal Research* 149(1–2), pages 85–102. ISSN: 0377-0273. DOI: 10.1016/j.jvolgeores.2005.06.002.

Bachmann, O., C. D. Deering, P. W. Lipman, and C. Plummer (2014). "Building zoned ignimbrites by recycling silicic cumulates: insight from the $1,000\,km^3$ Carpenter Ridge Tuff, CO". *Contributions to Mineralogy and Petrology* 167(6). ISSN: 1432-0967. DOI: 10.1007/s00410-014-1025-3.

Bachmann, O., M. A. Dungan, and P. W. Lipman (2002). "The Fish Canyon magma body, San Juan Volcanic Field, Colorado: Rejuvenation and eruption of an upper-crustal batholith". *Journal of Petrology* 43(8), pages 1469–1503. ISSN: 1460-2415. DOI: 10.1093/petrology/43.8.1469.

Bain, A. A., A. M. Jellinek, and R. A. Wiebe (2013). "Quantitative field constraints on the dynamics of silicic magma chamber rejuvenation and overturn". *Contributions to Mineralogy and Petrology* 165(6), pages 1275–1294. ISSN: 1432-0967. DOI: 10.1007/s00410-013-0858-5.

Bergantz, G. W. (1989). "Underplating and partial melting: Implications for melt generation and extraction". *Science* 245(4922), pages 1093–1095. ISSN: 1095-9203. DOI: 10.1126/science.245.4922.1093.

Bergantz, G. W. and R. E. Breidenthal (2001). "Non-stationary entrainment and tunneling eruptions: A dynamic link between eruption processes and magma mixing". *Geophysical Research Letters* 28(16), pages 3075–3078. ISSN: 1944-8007. DOI: 10.1029/2001gl013304.

Bergantz, G. W., J. M. Schleicher, and A. Burgisser (2015). "Open-system dynamics and mixing in magma mushes". *Nature Geoscience* 8(10), pages 793–796. ISSN: 1752-0908. DOI: 10.1038/ngeo2534.

Bergantz, G. W., J. M. Schleicher, and A. Burgisser (2017). "On the kinematics and dynamics of crystal-rich systems". *Journal of Geophysical Research: Solid Earth* 122(8), pages 6131–6159. ISSN: 2169-9356. DOI: 10.1002/2017jb014218.

Boudreau, A. (1999). "PELE-a version of the MELTS software program for the PC platform". *Computers & Geosciences* 25(2), pages 201–203. ISSN: 0098-3004. DOI: 10.1016/s0098-3004(98)00117-4.

Burgisser, A. and G. W. Bergantz (2011). "A rapid mechanism to remobilize and homogenize highly crystalline magma bodies". *Nature* 471(7337), pages 212–215. ISSN: 1476-4687. DOI: 10.1038/nature09799.

Burgisser, A., A. Carrara, and C. Annen (2020). "Numerical simulations of magmatic enclave deformation". *Journal of Volcanology and Geothermal Research* 392, page 106790. ISSN: 0377-0273. DOI: 10.1016/j.jvolgeores.2020.106790.

Caricchi, L. and J. Blundy (2015). "Experimental petrology of monotonous intermediate magmas". *Geological Society, London, Special Publications* 422(1), pages 105–130. ISSN: 2041-4927. DOI: 10.1144/sp422.9.

Carrara, A. (2019). "Numerical modeling of the physical processes causing the reawakening of a magmatic chamber and of the associated geophysical signals". Ph.D. Thesis. Université Grenoble Alpes.

Carrara, A., A. Burgisser, and G. W. Bergantz (2020). "The architecture of intrusions in magmatic mush". *Earth and Planetary Science Letters* 549, page 116539. ISSN: 0012-821X. DOI: 10.1016/j.epsl.2020.116539.

Clynne, M. A. (1999). "A complex magma mixing origin for rocks erupted in 1915, Lassen Peak, California". *Journal of Petrology* 40(1), pages 105–132. ISSN: 1460-2415. DOI: 10.1093/petroj/40.1.105.

Couch, S., R. S. J. Sparks, and M. R. Carroll (2001). "Mineral disequilibrium in lavas explained by convective self-mixing in open magma chambers". *Nature* 411(6841), pages 1037–1039. ISSN: 1476-4687. DOI: 10.1038/35082540.

Culha, C., J. Suckale, T. Keller, and Z. Qin (2020). "Crystal fractionation by crystal-driven convection". *Geophysical Research Letters* 47(4). ISSN: 1944-8007. DOI: 10.1029/2019gl086784.

Dufek, J. and O. Bachmann (2010). "Quantum magmatism: Magmatic compositional gaps generated by melt–crystal dynamics". *Geology* 38(8), pages 687–690. ISSN: 0091-7613. DOI: 10.1130/g30831.1.

Eichelberger, J. C. and P. E. Izbekov (2000). "Eruption of andesite triggered by dyke injection: contrasting cases at Karymsky Volcano, Kamchatka and Mt Katmai, Alaska". *Philosophical Transactions of the Royal Society of London. Series A: Mathematical, Physical and Engineering Sciences* 358(1770), pages 1465–1485. ISSN: 1471-2962. DOI: 10.1098/rsta.2000.0599.

Garg, R., J. Galvin, T. Li, and S. Pannala (2012). "Open-source MFIX–DEM software for gas—solids flows: Part I—Verification studies". *Powder Technology* 220, pages 122–137. ISSN: 0032-5910. DOI: 10.1016/j.powtec.2011.09.019.

Ghiorso, M. S. and R. O. Sack (1995). "Chemical mass transfer in magmatic processes IV. A revised and internally consistent thermodynamic model for the interpolation and extrapolation of liquid–solid equilibria in magmatic systems at elevated temperatures and pressures". *Contributions to Mineralogy and Petrology* 119(2–3), pages 197–212. ISSN: 1432-0967. DOI: 10.1007/bf00307281.

Giordano, D., J. K. Russell, and D. B. Dingwell (2008). "Viscosity of magmatic liquids: A model". *Earth and Planetary Science Letters* 271(1–4), pages 123–134. ISSN: 0012-821X. DOI: 10.1016/j.epsl.2008.03.038.

Huber, C., O. Bachmann, and J. Dufek (2011). "Thermo-mechanical reactivation of locked crystal mushes: Melting-induced internal fracturing and assimilation processes in magmas". *Earth and Planetary Science Letters* 304(3–4), pages 443–454. ISSN: 0012-821X. DOI: 10.1016/j.epsl.2011.02.022.

Huber, C., O. Bachmann, and M. Manga (2009). "Homogenization processes in silicic magma chambers by stirring and mushification (latent heat buffering)". *Earth and Planetary Science Letters* 283(1–4), pages 38–47. ISSN: 0012-821X. DOI: 10.1016/j.epsl.2009.03.029.

Huppert, H. E., R. S. J. Sparks, and J. S. Turner (1982). "Effects of volatiles on mixing in calc-alkaline magma systems". *Nature* 297(5867), pages 554–557. ISSN: 1476-4687. DOI: 10.1038/297554a0.

Jarvis, P. A., H. M. Mader, H. E. Huppert, K. V. Cashman, and J. D. Blundy (2019). "Experiments on the low-Reynolds-number settling of a sphere through a fluid interface". *Physical Review Fluids* 4(2). ISSN: 2469-990X. DOI: 10.1103/physrevfluids.4.024003.

Jarvis, P. A., M. Pistone, A. Secretan, J. D. Blundy, K. V. Cashman, H. M. Mader, and L. P. Baumgartner (2021). "Crystal and volatile controls on the mixing and mingling of magmas". *Crustal magmatic system evolution: Anatomy, architecture, and physico-chemical processes*. Edited by M. Masotta, C. Beier, and S. Mollo. Geophysical Monograph Series. American Geophysical Union. Chapter 6, pages 125–150. ISBN: 9781119564485. DOI: 10.1002/9781119564485.ch6.

Jellinek, A. M. and R. C. Kerr (1999). "Mixing and compositional stratification produced by natural convection: 2. Applications to the differentiation of basaltic and silicic magma chambers and komatiite lava flows". *Journal of Geophysical Research: Solid Earth* 104(B4), pages 7203–7218. ISSN: 0148-0227. DOI: 10.1029/1998jb900117.

Jellinek, A. M., R. C. Kerr, and R. W. Griffiths (1999). "Mixing and compositional stratification produced by natural convection: 1. Experiments and their application to Earth's core and mantle". *Journal of Geophysical Research: Solid Earth* 104(B4), pages 7183–7201. ISSN: 0148-0227. DOI: 10.1029/1998jb900116.

Karakas, O., W. Degruyter, O. Bachmann, and J. Dufek (2017). "Lifetime and size of shallow magma bodies controlled by crustal-scale magmatism". *Nature Geoscience* 10(6), pages 446–450. ISSN: 1752-0908. DOI: 10.1038/ngeo2959.

Laumonier, M., B. Scaillet, M. Pichavant, R. Champallier, J. Andujar, and L. Arbaret (2014). "On the conditions of magma mixing and its bearing on andesite production in the crust". *Nature Communications* 5(1). ISSN: 2041-1723. DOI: 10.1038/ncomms6607.

Leuthold, J., O. Müntener, L. P. Baumgartner, B. Putlitz, M. Ovtcharova, and U. Schaltegger (2012). "Time resolved construction of a bimodal laccolith (Torres del Paine, Patagonia)". *Earth and Planetary Science Letters* 325–326, pages 85–92. ISSN: 0012-821X. DOI: 10.1016/j.epsl.2012.01.032.

Li, T., R. Garg, J. Galvin, and S. Pannala (2012). "Open-source MFIX–DEM software for gas–solids flows: Part II—Validation studies". *Powder Technology* 220, pages 138–150. ISSN: 0032-5910. DOI: 10.1016/j.powtec.2011.09.020.

Melekhova, E., C. Annen, and J. Blundy (2013). "Compositional gaps in igneous rock suites controlled by magma system heat and water content". *Nature Geoscience* 6(5), pages 385–390. ISSN: 1752-0908. DOI: 10.1038/ngeo1781.

Michel, J., L. Baumgartner, B. Putlitz, U. Schaltegger, and M. Ovtcharova (2008). "Incremental growth of the Patagonian Torres del Paine laccolith over 90 k.y." *Geology* 36(6), page 459. ISSN: 0091-7613. DOI: 10.1130/g24546a.1.

Molina, I., A. Burgisser, and C. Oppenheimer (2012). "Numerical simulations of convection in crystal-bearing magmas: A case study of the magmatic system at Erebus, Antarctica". *Journal of Geophysical Research: Solid Earth* 117(B7). ISSN: 0148-0227. DOI: 10.1029/2011jb008760.

Montagna, C. P., P. Papale, and A. Longo (2015). "Timescales of mingling in shallow magmatic reservoirs". *Geological Society, London, Special Publications* 422(1), pages 131–140. ISSN: 2041-4927. DOI: 10.1144/sp422.6.

Murphy, M. D., R. S. J. Sparks, J. Barclay, M. R. Carroll, and T. S. Brewer (2000). "Remobilization of andesite magma by intrusion of mafic magma at the Soufriere Hills Volcano, Montserrat, West Indies". *Journal of Petrology* 41(1), pages 21–42. ISSN: 0022-3530. DOI: 10.1093/petrology/41.1.21.

Nakagawa, M., K. Wada, and C. P. Wood (2002). "Mixed Magmas, Mush Chambers and Eruption Triggers: Evidence from Zoned Clinopyroxene Phenocrysts in Andesitic Scoria from the 1995 Eruptions of Ruapehu Volcano, New Zealand". *Journal of Petrology* 43(12), pages 2279–2303. ISSN: 1460-2415. DOI: 10.1093/petrology/43.12.2279.

Ottino, J. M. (1989). *The kinematics of mixing: stretching, chaos, and transport.* Volume 3. Cambridge University Press.

Pallister, J. S., R. P. Hoblitt, G. P. Meeker, R. J. Knight, and D. F. Siems (1996). "Magma mixing at Mount Pinatubo: petrographic and chemical evidence from the 1991 deposits". *Fire and mud: eruptions and lahars of Mount Pinatubo, Philippines*. Edited by C. G. Newhall and R. S. Punongbayan. Philippine Institute of Volcanology, Seismology, and University of Washington Press, pages 687–731.

Parmigiani, A., W. Degruyter, S. Leclaire, C. Huber, and O. Bachmann (2017). "The mechanics of shallow magma reservoir outgassing". *Geochemistry, Geophysics, Geosystems* 18(8), pages 2887–2905. ISSN: 1525-2027. DOI: 10.1002/2017gc006912.

Parmigiani, A., C. Huber, and O. Bachmann (2014). "Mush microphysics and the reactivation of crystal-rich magma reservoirs". *Journal of Geophysical Research: Solid Earth* 119(8), pages 6308–6322. ISSN: 2169-9356. DOI: 10.1002/2014jb011124.

Perugini, D. and G. Poli (2005). "Viscous fingering during replenishment of felsic magma chambers by continuous inputs of mafic magmas: Field evidence and fluid-mechanics experiments". *Geology* 33(1), page 5. ISSN: 0091-7613. DOI: 10.1130/g21075.1.

Pichavant, M., S. Poussineau, P. Lesne, C. Solaro, and J.-L. Bourdier (2018). "Experimental parametrization of magma mixing: Application to the AD 1530 eruption of La Soufrière, Guadeloupe (Lesser Antilles)". *Journal of Petrology* 59(2), pages 257–282. ISSN: 1460-2415. DOI: 10.1093/petrology/egy030.

Renggli, C. J., S. Wiesmaier, C. P. De Campos, K.-U. Hess, and D. B. Dingwell (2016). "Magma mixing induced by particle settling". *Contributions to Mineralogy and Petrology* 171(11). ISSN: 1432-0967. DOI: 10.1007/s00410-016-1305-1.

Ruprecht, P., G. W. Bergantz, and J. Dufek (2008). "Modeling of gas-driven magmatic overturn: Tracking of phenocryst dispersal and gathering during magma mixing". *Geochemistry, Geophysics, Geosystems* 9(7). ISSN: 1525-2027. DOI: 10.1029/2008gc002022.

Schleicher, J. M., G. W. Bergantz, R. E. Breidenthal, and A. Burgisser (2016). "Time scales of crystal mixing in magma mushes". *Geophysical Research Letters* 43(4), pages 1543–1550. ISSN: 1944-8007. DOI: 10.1002/2015gl067372.

Snyder, D. (2000). "Thermal effects of the intrusion of basaltic magma into a more silicic magma chamber and implications for eruption triggering". *Earth and Planetary Science Letters* 175(3–4), pages 257–273. ISSN: 0012-821X. DOI: 10.1016/s0012-821x(99)00301-5.

Snyder, D. and S. Tait (1995). "Replenishment of magma chambers: comparison of fluid-mechanic experiments with field relations". *Contributions to Mineralogy and Petrology* 122(3), pages 230–240. ISSN: 1432-0967. DOI: 10.1007/s004100050123.

– (1996). "Magma mixing by convective entrainment". *Nature* 379(6565), pages 529–531. ISSN: 1476-4687. DOI: 10.1038/379529a0.

Syamlal, M. (1998). *MFIX documentation numerical technique.* DOI: 10.2172/656644.

Syamlal, M., W. Rogers, and T. O'Brien (1993). *MFIX documentation theory guide.* DOI: 10.2172/10145548.

Takahashi, R. and M. Nakagawa (2013). "Formation of a compositionally reverse zoned magma chamber: Petrology of the AD 1640 and 1694 eruptions of Hokkaido–Komagatake Volcano, Japan". *Journal of Petrology* 54(4), pages 815–838. ISSN: 0022-3530. DOI: 10.1093/petrology/egs087.

Thomas, N. and S. Tait (1997). "The dimensions of magmatic inclusions as a constraint on the physical mechanism of mixing". *Journal of Volcanology and Geothermal Research* 75(1–2), pages 167–178. ISSN: 0377-0273. DOI: 10.1016/s0377-0273(96)00034-0.

Wiebe, R. A. (1996). "Mafic–silicic layered intrusions: the role of basaltic injections on magmatic processes and the evolution of silicic magma chambers". *Earth and Environmental Science Transactions of the Royal Society of Edinburgh* 87(1–2), pages 233–242. ISSN: 1755-6929. DOI: 10.1017/s0263593300006647.

– (2016). "Mafic replenishments into floored silicic magma chambers". *American Mineralogist* 101(2), pages 297–310. ISSN: 0003-004X. DOI: 10.2138/am-2016-5429.

Wiesmaier, S., D. Morgavi, C. J. Renggli, D. Perugini, C. P. De Campos, K.-U. Hess, W. Ertel-Ingrisch, Y. Lavallée, and D. B. Dingwell (2015). "Magma mixing enhanced by bubble segregation". *Solid Earth* 6(3), pages 1007–1023. ISSN: 1869-9529. DOI: 10.5194/se-6-1007-2015.